Supporting information

Improving bottom-up ammonia emission inventory estimations in Guangdong combining ammonia measurements from a ground-based network and FY-4B satellite and GCHP model

Lingze Meng[1,2], Ni Lu[1], Yixin Guo[1], Ziru Lan[1], Zhao-Cheng Zeng[3], Zichong Chen[1,4], Yuanhong Zhao[5,6], Zhuangmin Zhong[2,7], Tao Zhang[2,7], Duohong Chen[2,7], Xuejun Liu[8], Lin Zhang[9], Junyu Zheng[10]

[1] Earth, Ocean and Atmospheric Sciences Thrust, Function Hub, Hong Kong University of Science & Technology (Guangzhou), Guangzhou 511442, China

[2] Key Laboratory of Regional Air Quality Monitoring, Ministry of Ecology and Environment, Guangzhou 510060, China

[3] School of Earth and Space Sciences, Peking University, Beijing 100871, China

[4] Thrust of Carbon Neutrality and Climate Change, Society Hub, Hong Kong University of Science & Technology (Guangzhou), Guangzhou 511442, China

[5] State Key Laboratory of Physical Oceanography, Ocean University of China, Qingdao 266100, China

[6] College of Oceanic and Atmospheric Sciences, Ocean University of China, Qingdao, 266100, China

[7] Guangdong Ecological and Environmental Monitoring Center, Guangzhou 510060, China

[8] State Key Laboratory of Nutrient Use and Management, College of Resources and Environmental Sciences, National Academy of Agriculture Green Development, National Observation and Research Station of Agriculture Green Development (Quzhou, Hebei), China Agricultural University, Beijing 100193, China

[9] Laboratory for Climate and Ocean-Atmosphere Studies, Department of Atmospheric and Oceanic Sciences, School of Physics, Peking University, Beijing 100871, People's Republic of China

[10] Sustainable Energy and Environment Thrust, Function Hub, Hong Kong University of Science & Technology (Guangzhou), Guangzhou 511442, China

Corresponding authors. E-mail address: Yixin Guo, yixinguo@hkust-gz.edu.cn

Contents of this file

Text S1. Detailed configurations of the GCHP model

GCHP simulations were performed with the standard full-chemistry configuration, allowing for explicit representation for processes relevant for NH_3, including transport, secondary inorganic aerosol formation, and deposition. The chemical mechanism includes gas-phase HO_x-NO_x-BrO_x-VOC-O_3 chemistry (Bey et al., 2001; Wang et al., 2021), together with aerosol modules for sulfate-nitrate-ammonium (Park et al., 2004), black carbon (Wang et al., 2014), dust (Fairlie et al., 2007), organic aerosols (Pai et al., 2020), and sea salt (Jaeglé et al., 2011). Gas-particle partitioning of inorganic aerosols is calculated with the HETP v1.0 thermodynamic module (Miller et al., 2024). Dry and wet deposition are both included in the simulation, with dry deposition represented by a resistance-in-series scheme and wet deposition including scavenging by convection and large-scale precipitation (Liu et al., 2001; Wang et al., 1998).

Simulations were performed for the year 2023 with a four-month spin-up for September to December of the previous year. Meteorological fields were provided by the Modern-Era Retrospective analysis for Research and Applications, Version 2 (MERRA-2) reanalysis (Gelaro et al., 2017). The model used 72 vertical layers and a 300s transport time step. We applied a C90 stretched-grid configuration with a stretch factor of 10.0 centered at 23.5 °N, 113.5 °E, yielding an effective horizontal resolution of approximately 0.1° × 0.1° over Guangdong. Anthropogenic emissions in the rest of China were from the Multi-resolution Emission Inventory model for Climate and air pollution research (MEIC) (Geng et al., 2024) for the year 2023, and emissions outside China were taken from the Community Emissions Data System (CEDS) for the year 2019 (Hoesly et al., 2018). Anthropogenic emissions within Guangdong were taken directly from GD-EI (Huang et al., 2012), as described in main text. All baseline, perturbation, posterior, and source-removal simulations used the same meteorology, chemistry, deposition schemes, and non-NH_3 emissions; only NH_3 emissions were varied according to each experiment. Model outputs were archived as hourly and monthly mean fields as needed for satellite column-to-surface conversion, station-based model evaluation, and inversion.

Text S2. Ground-based measurements and model evaluation metrics

Ambient NH_3 at the PRD monitoring sites was measured using active chemiluminescence ammonia analyzers (Model 17i, Thermo Fisher Scientific, USA), which quantify NH_3 by thermal conversion to NO followed by chemiluminescent detection of the reaction between nitric oxide (NO) and ozone (O_3). The instrument is U.S. EPA verified, with a lower detectable limit of 1.0 ppb and a stated precision of ±0.3 μg m^{-3}. Routine QA/QC included zero/span checks, multipoint calibration, linearity tests, and converter-efficiency verification.

In addition to NH_3, particulate NH_4^+, SO_4^{2-} and NO_3^- measurements from the PRD monitoring network were used to evaluate whether GCHP reasonably reproduced the chemical environment controlling NH_3-NH_4^+ partitioning and secondary inorganic aerosol formation. The PRD monitoring network includes six sites that provide hourly particulate ion observations (Figure S1 and Table S1). At these sites, particulate NH_4^+, SO_4^{2-} and NO_3^- were measured using online aerosol ion chromatography systems (Metrohm 2060 MARGA and TH-GAC-IC3000), which combine a wet rotating denuder and a steam-jet aerosol collector with ion chromatography for simultaneous hourly observations. We also used $PM_{2.5}$ and O_3 observations from the China National Environmental Monitoring Centre (CNEMC; https://air.cnemc.cn:18007/) to evaluate the model performance for major air pollutants relevant to secondary aerosol formation.

Hourly observations from the PRD ion-monitoring sites and CNEMC were aggregated to monthly means and compared with monthly mean GCHP outputs sampled at the corresponding locations. Agreement for these non-NH_3 constraints helps show that the model chemistry and prior emissions for species other than NH_3 are not the dominant sources of bias in the NH_3 inversion framework. Specifically, we use the normalized mean bias (NMB) and normalized root mean square error (NRMSE) to quantify the model performance. These metrics were also used to compare the prior and posterior GCHP simulations with the corrected FY-4B-ground surface NH_3 observational constraint. NMB measures the mean signed bias of the model relative to observations. A positive NMB indicates model overestimation, whereas a negative NMB indicates model underestimation. NMB was calculated as follows:

$$NMB = \frac{\sum_{i=1}^{n}(M_i - y_i)}{\sum_{i=1}^{n} y_i} \times 100\%$$

where M_i and y_i are the modeled and observed values for grid cell i, respectively, and n is the total number of paired model-observation grid cells.

NRMSE measures the magnitude of the model-observation discrepancy after normalization by the mean observed value. Compared with NMB, which reflects the direction of the mean bias, NRMSE provides an estimate of the overall relative error and is less affected by compensation between positive and negative errors. NRMSE was calculated as follows:

$$NRMSE = \frac{\sqrt{\frac{\sum_{i=1}^{n}(M_i - y_i)^2}{n}}}{\frac{1}{n}\sum_{i=1}^{n} y_i} \times 100\%$$

Text S3. Cost function and linearized sensitivity matrix

The objective of the Bayesian inversion is to find the posterior state vector that is most consistent with both the prior emission estimate and the observational constraints. This is achieved by minimizing a cost function, which combines a prior constraint term and an observational constraint term:

$$J(\mathbf{x}_{m,r}) = (\mathbf{x}_{m,r} - \mathbf{x}_{a,m,r})^T \mathbf{S}_{a,m,r}^{-1} (\mathbf{x}_{m,r} - \mathbf{x}_{a,m,r}) + \left(\mathbf{y}_{m,r} - \mathbf{F}(\mathbf{x}_{m,r})\right)^T \mathbf{S}_{o,m,r}^{-1} \left(\mathbf{y}_{m,r} - \mathbf{F}(\mathbf{x}_{m,r})\right)$$

Where $\mathbf{x}_{m,r}$ is the emission scaling-factor vector for month month m and region r, $\mathbf{x}_{a,m,r}$ is the prior state vector,

The posterior state vector corresponds to the minimum of $\boldsymbol{J}(\mathbf{x}_{m,r})$. Therefore, it satisfies the first-order optimality condition:

$$\nabla_{\mathbf{x}} J(\mathbf{x}_{m,r}) = 0$$

Where:

$$\nabla_{\mathbf{x}} J(\mathbf{x}_{m,r}) = 2\mathbf{S}_{a,m,r}^{-1}(\mathbf{x}_{m,r} - \mathbf{x}_{a,m,r}) + 2\mathbf{K}^T \mathbf{S}_{o,m,r}^{-1}(\mathbf{F}(\mathbf{x}_{m,r}) - \mathbf{y}_{m,r})$$

In this study, we approximate the model response as linear in the vicinity of the prior emissions. As a result, the Jacobian matrix $\mathbf{K}_{m,r}$ was estimated by linear regression using the perturbation simulations. This condition gives the analytical posterior solution:

$$\hat{\mathbf{x}}_{m,r} = \mathbf{x}_{a,m,r} + \left(\mathbf{K}_{m,r}^T \mathbf{S}_{o,m,r}^{-1} \mathbf{K}_{m,r} + \mathbf{S}_{a,m,r}^{-1}\right)^{-1} \mathbf{K}_{m,r}^T \mathbf{S}_{o,m,r}^{-1} (\mathbf{y}_{m,r} - \mathbf{K}_{m,r}\mathbf{x}_{a,m,r})$$

The validity of the Bayesian inversion depends on whether the linearized sensitivity matrix can approximate the full nonlinear GCHP response near the posterior solution. To test this assumption, we compared linearly reconstructed posterior NH_3 concentrations with an independent posterior GCHP rerun driven by the optimized emission inventory. As shown in Figure S9, linearized reconstructed posterior NH_3 (x-axis) means NH_3 concentrations calculated by using the sensitivity matrix derived from emission perturbation simulations multiplied by posterior state vector ($\mathbf{K}_{m,r}\hat{\mathbf{x}}_{m,r}$). The posterior simulated NH_3 (y-axis) refers to NH_3 concentrations from independent GCHP simulation driven by the posterior emission inventory ($\mathbf{F}(\hat{\mathbf{x}}_{m,r})$). Agreement between the two estimates indicates that the linearized response used in the inversion reasonably approximates the full nonlinear model response.

In Figure S9, the two estimates show a strong correspondence, with a fitted slope of 1.22, an NMB of 22.6 %, and an NRMSE of 31.7 %. This result suggests that the linearized response provides a reasonable approximation to the full nonlinear GCHP response, although remaining

differences may reflect nonlinear processes.

Text S4. Premature mortality calculation method

The premature deaths attributable to long-term $PM_{2.5}$ exposure were estimated using the Global Exposure Mortality Model (GEMM), a nonlinear hazard-ratio model constructed from cohort studies of outdoor $PM_{2.5}$ exposure and mortality.(Burnett et al., 2018) For each grid cell i, $PM_{2.5}$ exposure above the counterfactual concentration was calculated as:

$$z_i = \max(0, C_i - C_0), \quad C_0 = 2.4\ \mu\text{g m}^{-3}$$

where z_i is the $PM_{2.5}$ concentration above the counterfactual level, C_i is the $PM_{2.5}$ concentration in grid cell i, and C_0 is the counterfactual concentration. Concentrations below C_0 were assumed to produce no additional mortality risk.

The age-specific GEMM hazard ratio was calculated as:

$$HR_{i,a} = \exp\left[\frac{O_a \log_{10}(1 + z_i/1.6)}{1 + \exp[-(z_i - 15.5)/36.8]}\right]$$

where $HR_{i,a}$ is the hazard ratio in grid cell i and age group a, and O_a is the age-specific GEMM parameter.

The $PM_{2.5}$-attributable premature deaths in region R were then calculated as:

$$M_R = \sum_{i \in R} \sum_a m_a\,(P_i r_a)\left(1 - \frac{1}{HR_{i,a}}\right)$$

where M_R is the total $PM_{2.5}$-attributable premature deaths in region R, m_a is the age-specific baseline mortality rate, r_a is the population fraction of age group a; and $P_i r_a$ is the age-specific population in grid cell i. R denotes Guangdong Province (GD), the Pearl River Delta (PRD), or non-PRD.

Avoided premature deaths under a given scenario were calculated relative to the posterior scenario as:

$$\Delta M_R = M_{R,\text{Posterior}} - M_{R,\text{Scenario}}$$

where positive ΔM_R indicates fewer $PM_{2.5}$-attributable premature deaths than in the posterior scenario.

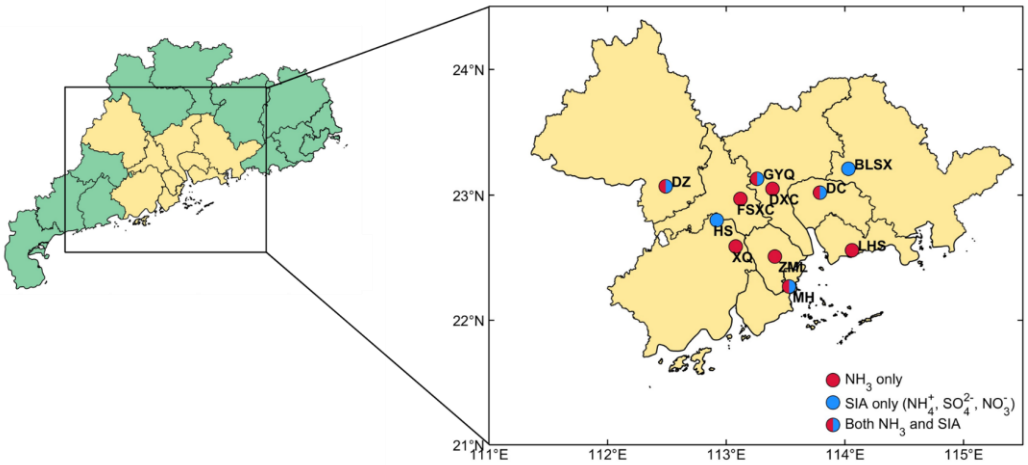

Figure S1. The ground-based ammonia observation network over Pearl River Delta (PRD) and site locations and measurement data for year 2023 utilized in this study given data availability and quality control. The left panel shows Guangdong Province, with PRD cities highlighted in yellow and non-PRD cities in green. The right panel shows the locations of sites within the PRD where red circles indicate sites with hourly NH_3 measurements and blue for sites with hourly particulate NH_4^+, SO_4^{2-} and NO_3^- measurements. Half-red half-blue circles indicate sites where both NH_3 and SIA measurements were available. The full name of each site is shown in Table S1.

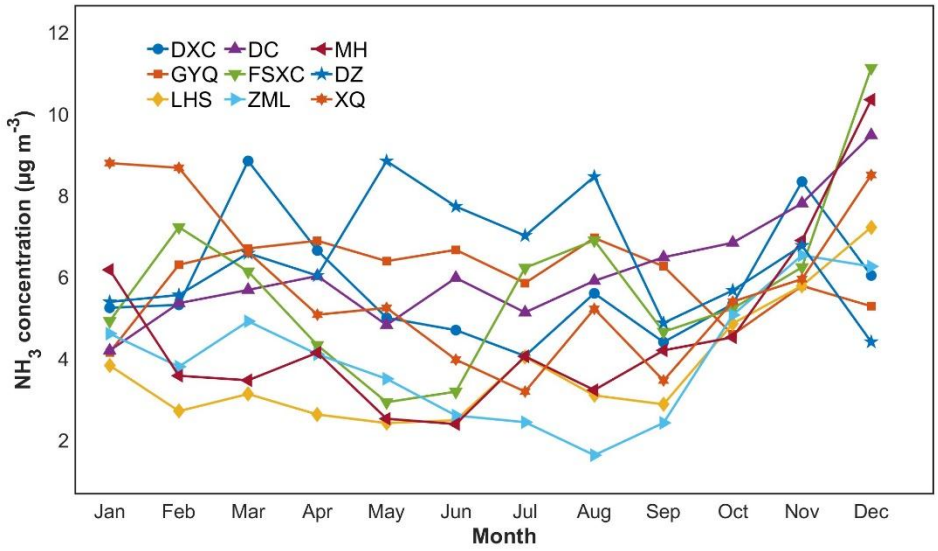

Figure S2. Monthly variation of NH_3 concentration in each site of Pearl River Delta (PRD) ground-based observation network in 2023.

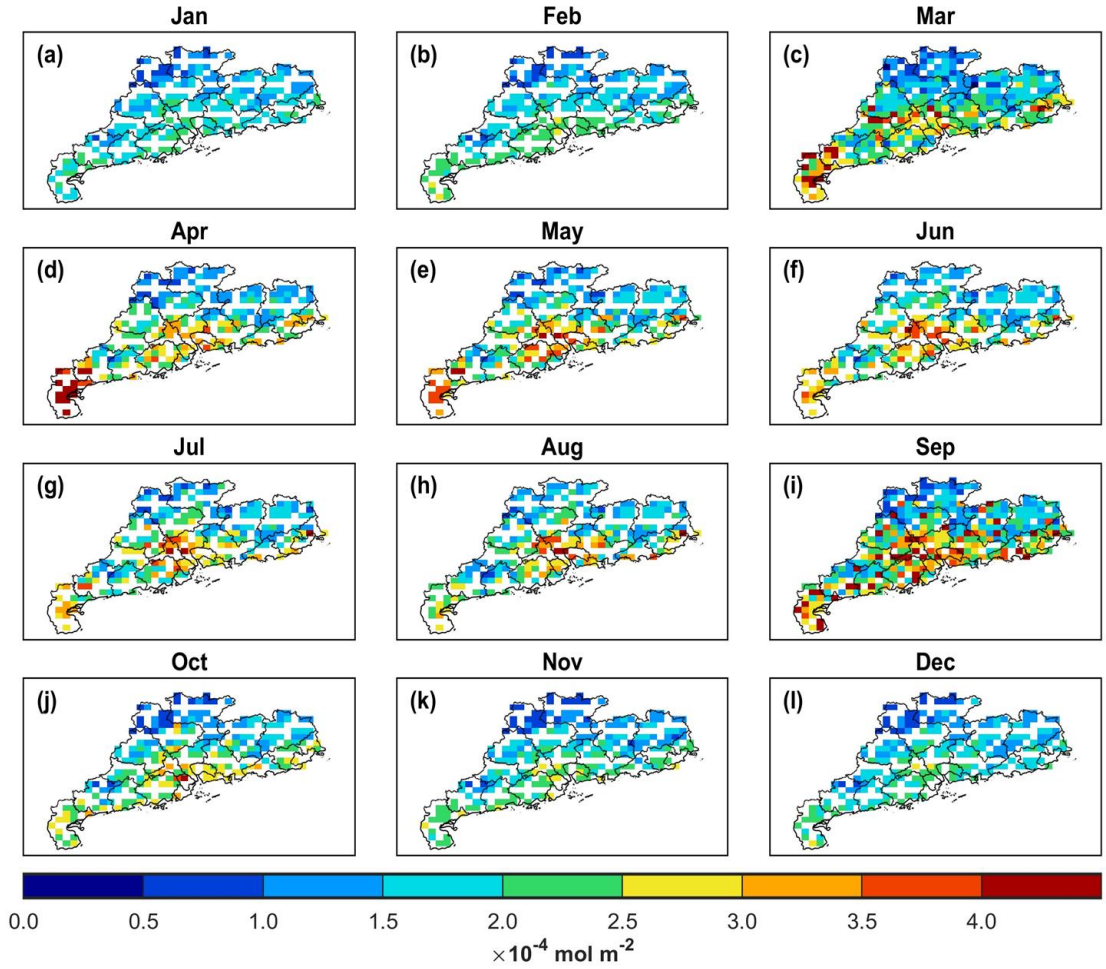

Figure S3. Spatial distributions of FY-4B NH_3 total column densities in China for different months of 2023

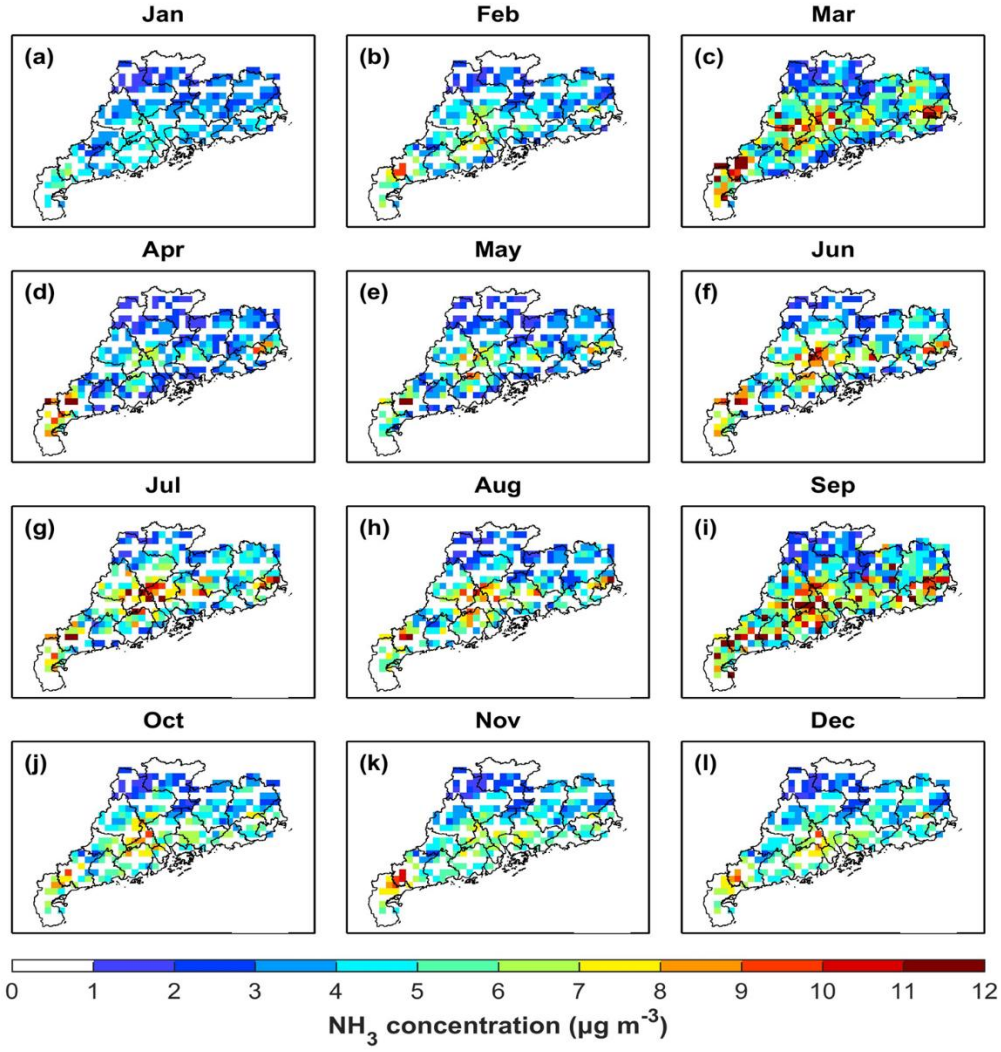

Figure S4. Monthly spatial distributions of FY-4B-derived surface NH_3 concentrations corrected by ground-based observations in 2023.

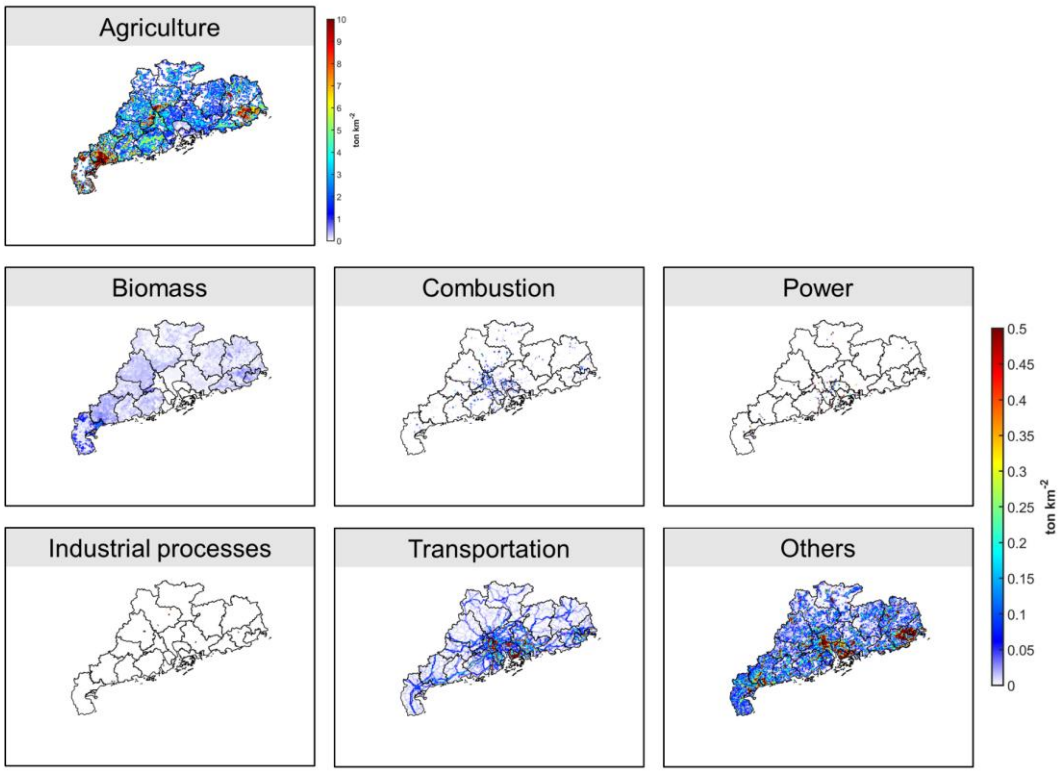

Figure S5. Spatial NH_3 emissions in the original GD-EI for 2023 from different sectors: (a) agriculture, (b) biomass, (c) combustion, (d) power, (e) industrial process, (f) transportation and (g) others

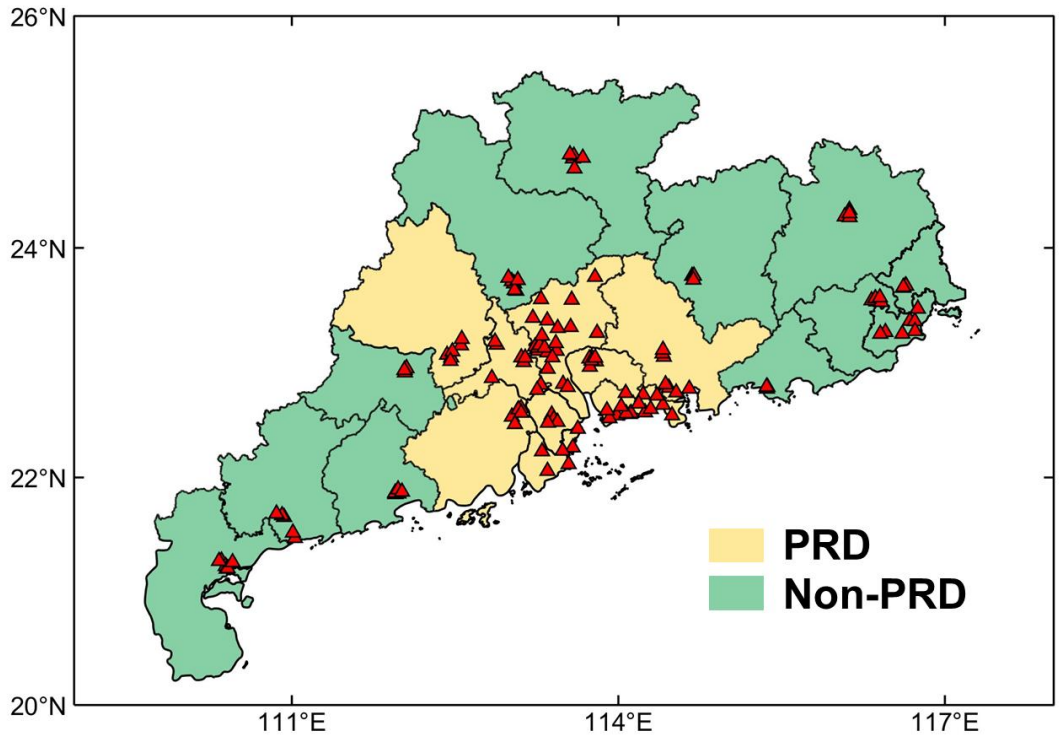

Figure S6. Distribution of ground monitoring sites from the China National Environmental Monitoring Centre (CNEMC) dataset used in this study over Guangdong Province.

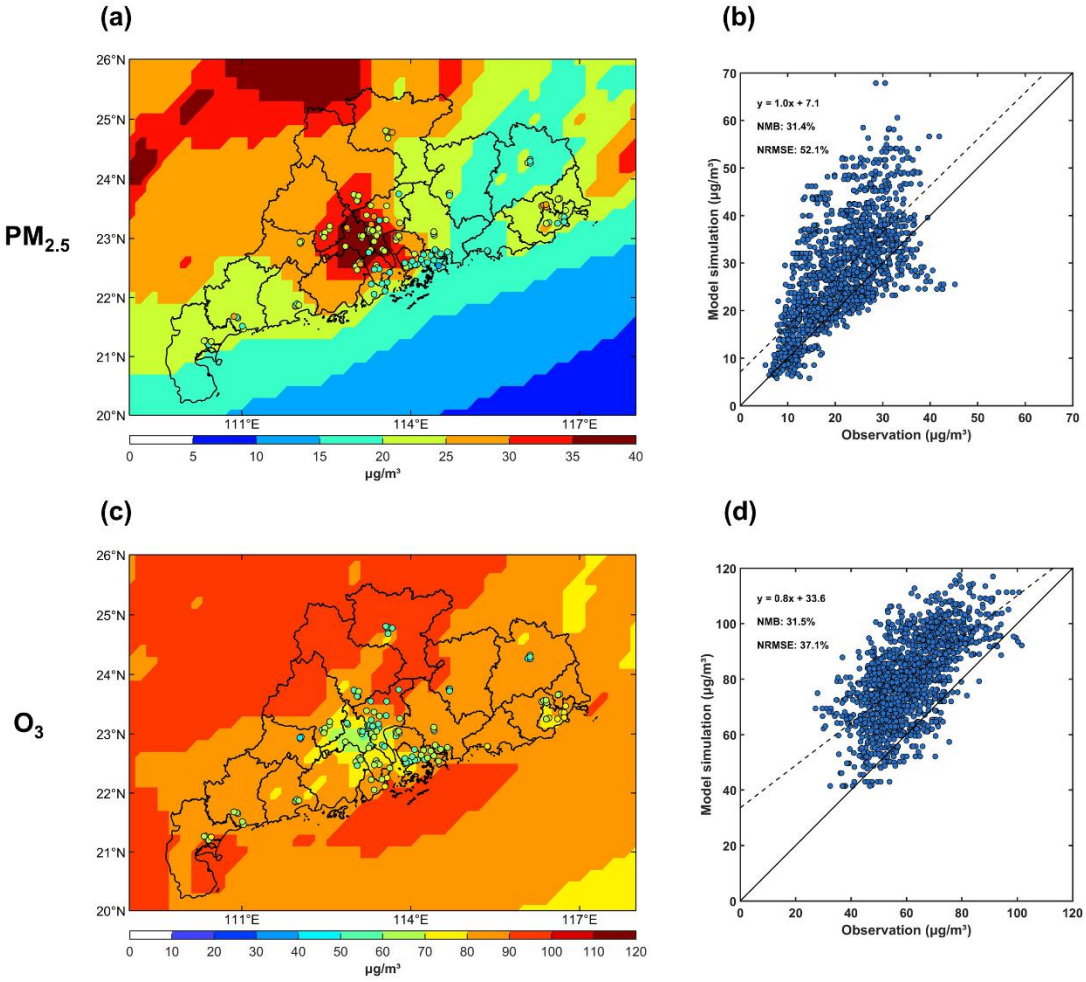

Figure S7. GCHP simulated surface $PM_{2.5}$ (a) and O_3 (c) concentrations using prior GD-EI over Guangdong in 2023, and their comparison with observations from the China National Environmental Monitoring Centre (CNEMC) dataset (b and d)

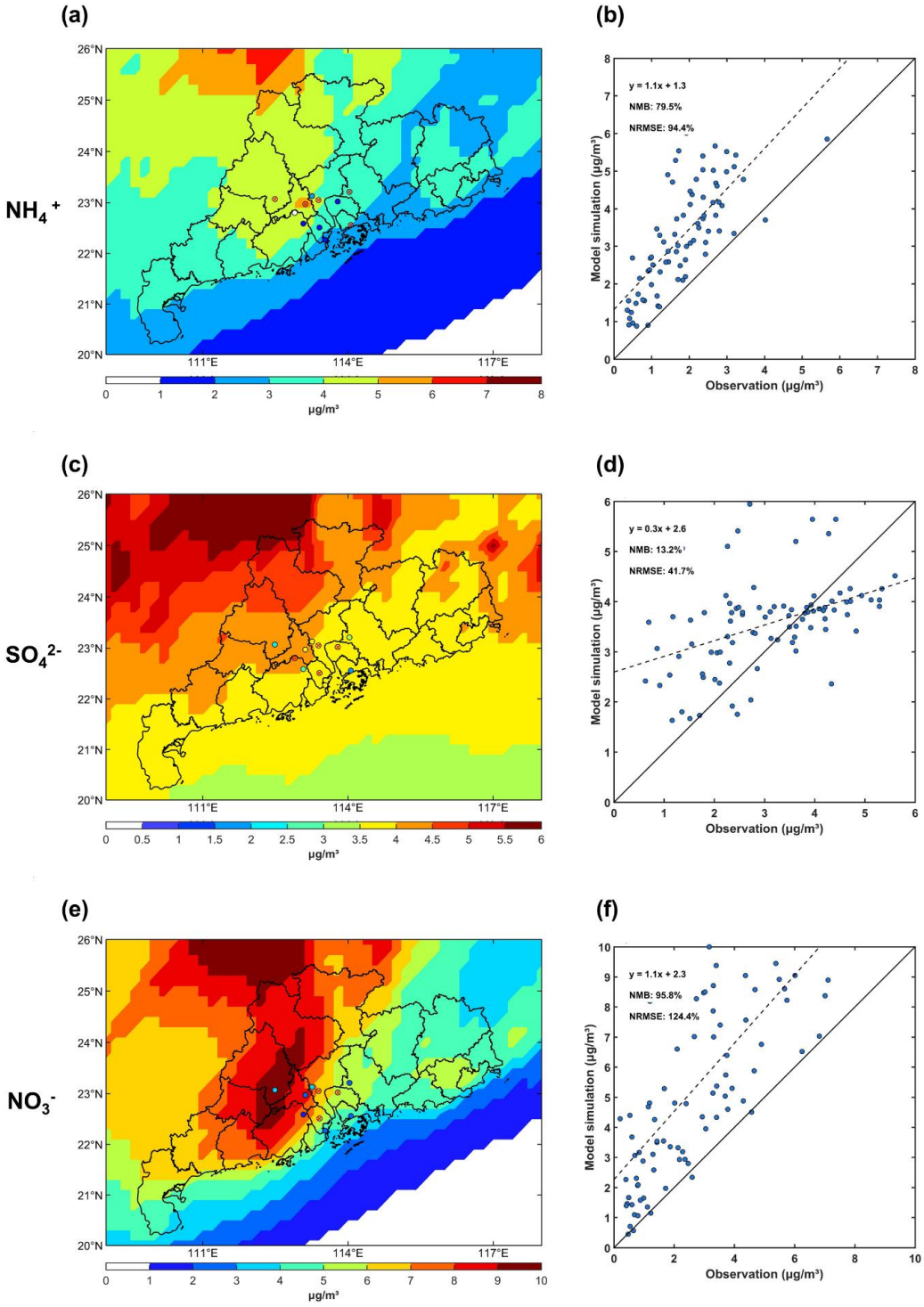

Figure S8. GCHP simulated surface NH_4^+ (a), SO_4^{2-} (c) and NO_3^- (e) concentrations using prior GD-EI over Guangdong in 2023, and their comparison with observations from the Pearl River Delta (PRD) monitoring network (b, d and f)

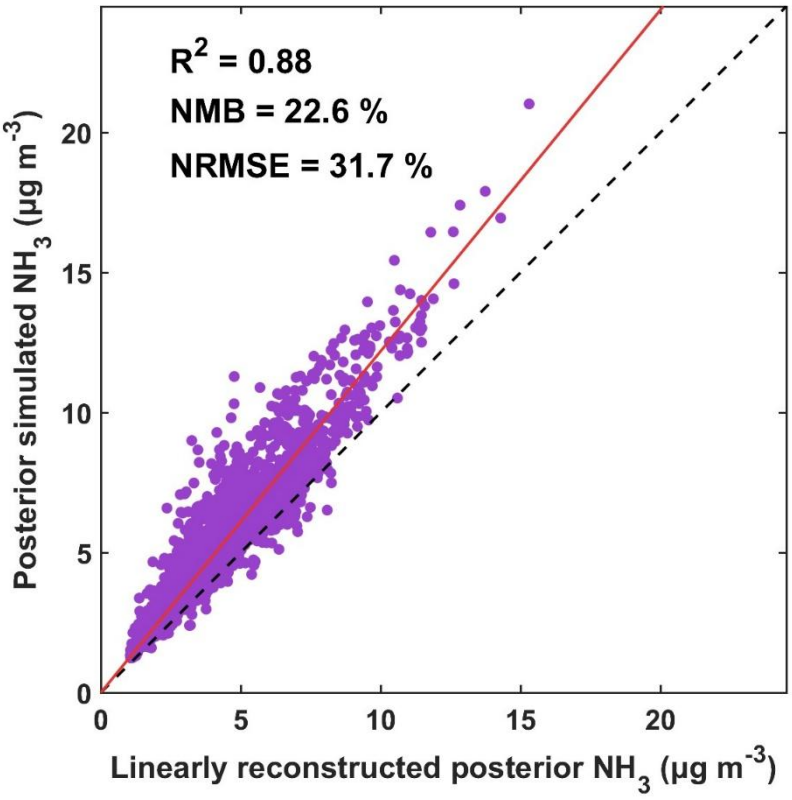

Figure S9. Evaluation of the linearized posterior NH_3 response against the full posterior GCHP simulation. The x-axis shows the linearly reconstructed posterior response, and the y-axis shows the independent GCHP simulation driven by posterior emissions. The dashed line indicates the 1:1 line.

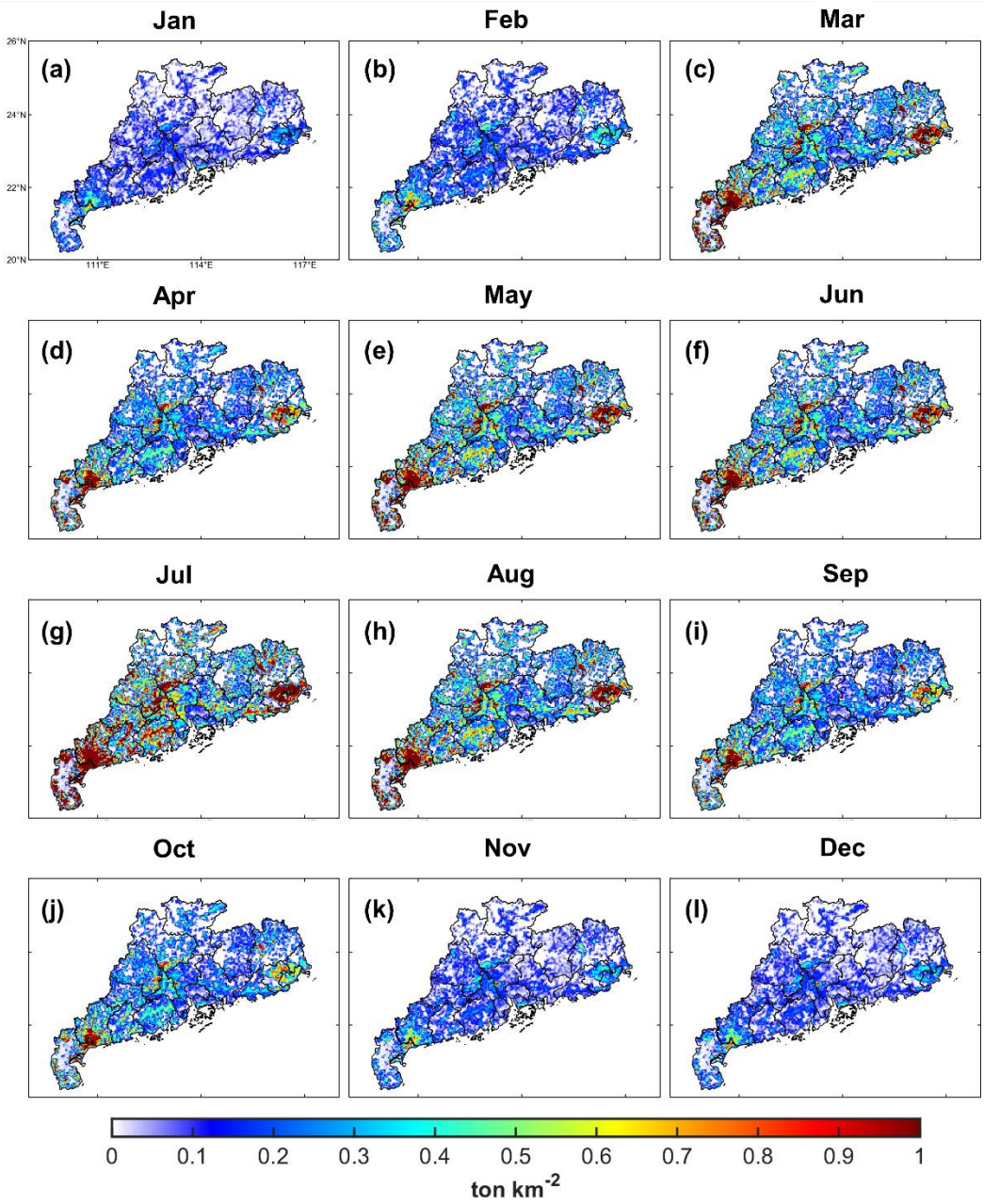

Figure S10. Monthly spatial distributions of prior NH_3 emissions in Guangdong Province in 2023

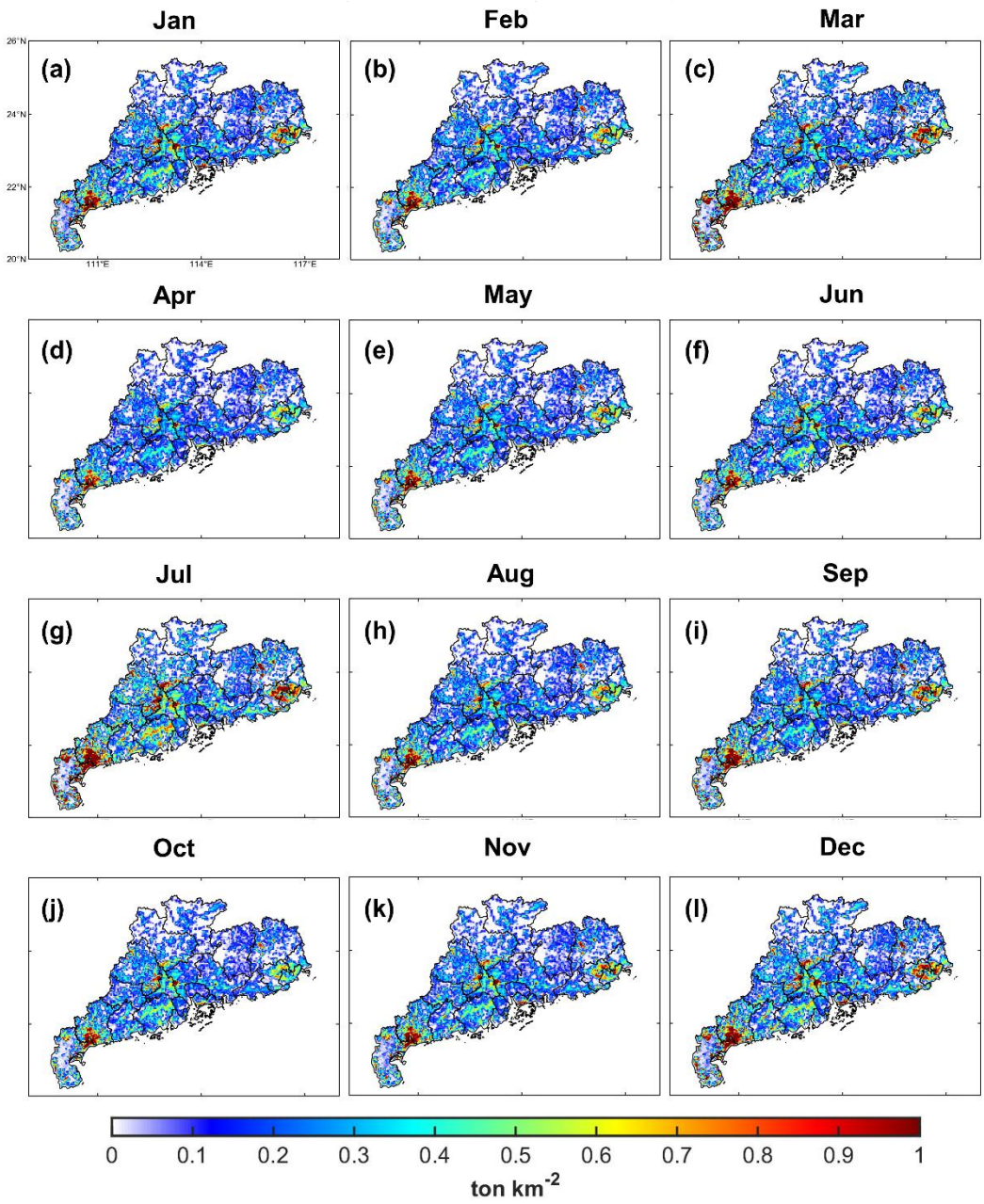

Figure S11. Monthly spatial distributions of posterior NH_3 emissions in Guangdong Province in 2023

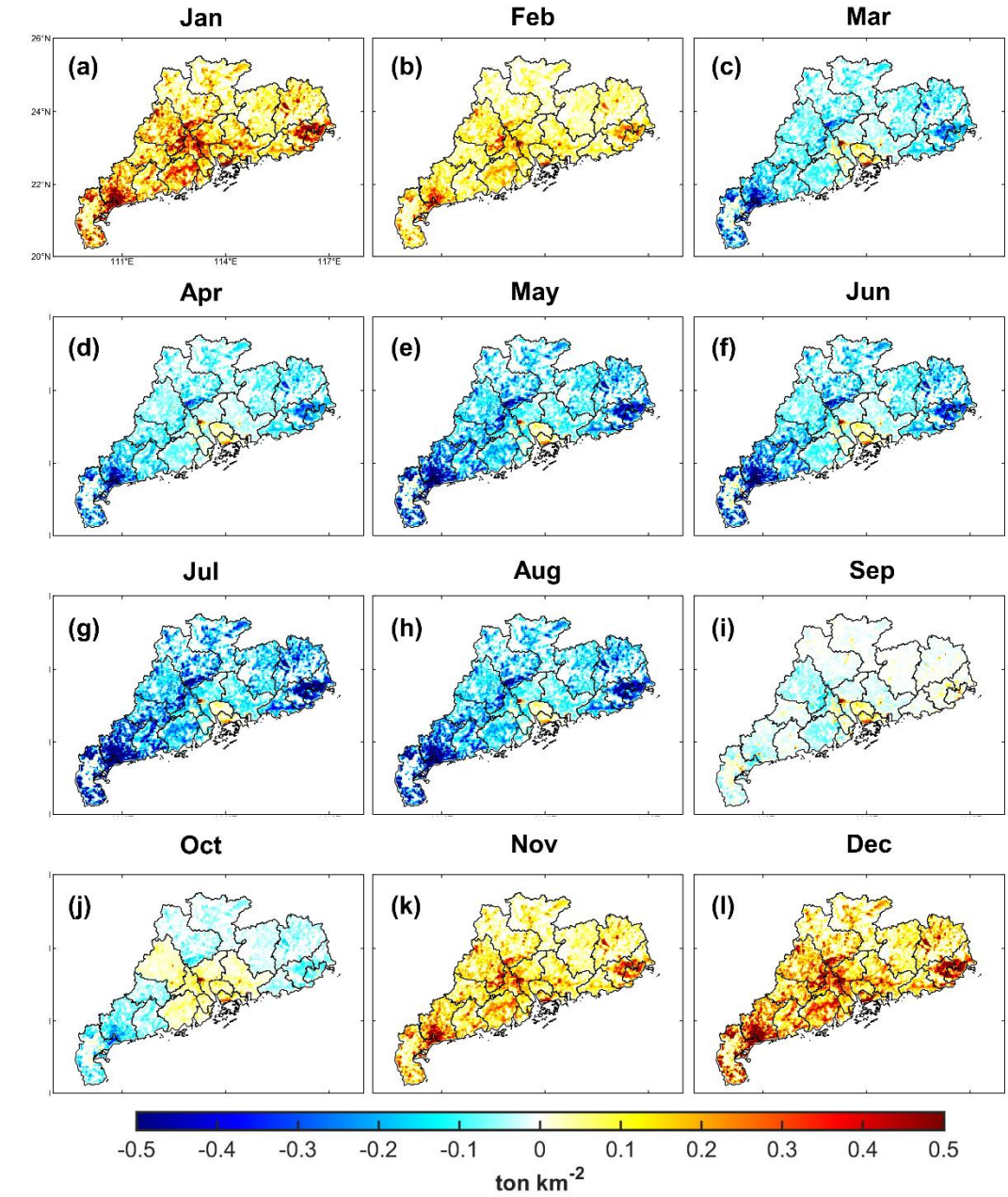

Figure S12. Monthly spatial distributions of posterior-minus-prior differences of NH_3 emissions in Guangdong Province in 2023

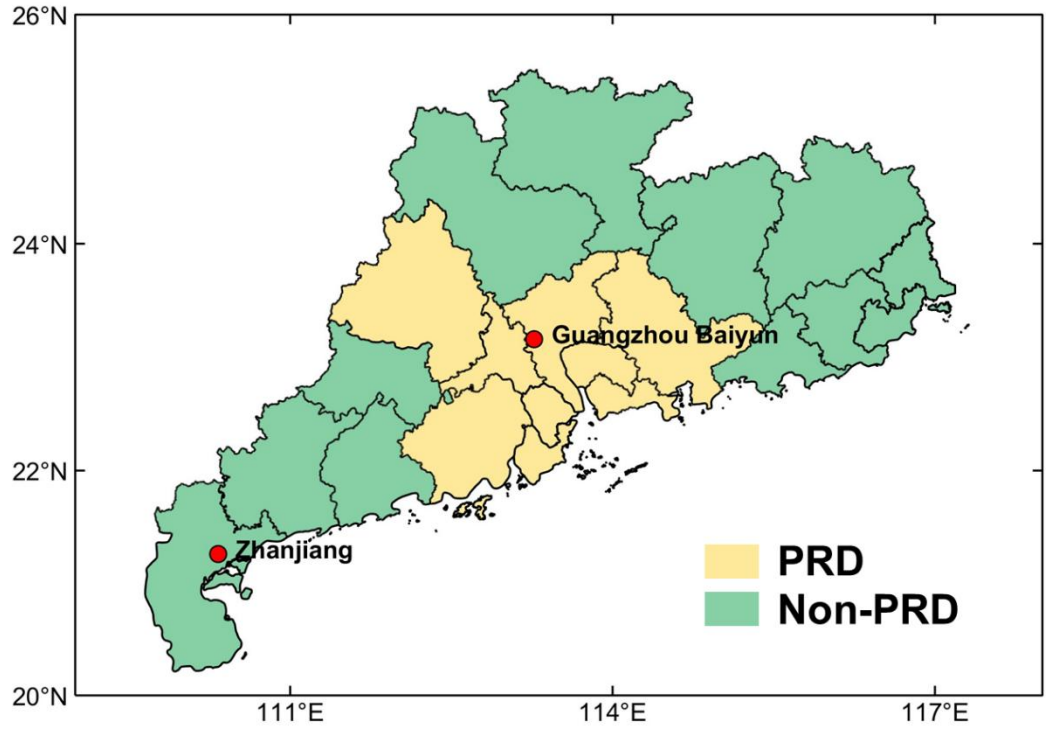

Figure S13. Distribution of the National Nitrogen Deposition Monitoring Network (NNDMN) sites used in this study over Guangdong Province.

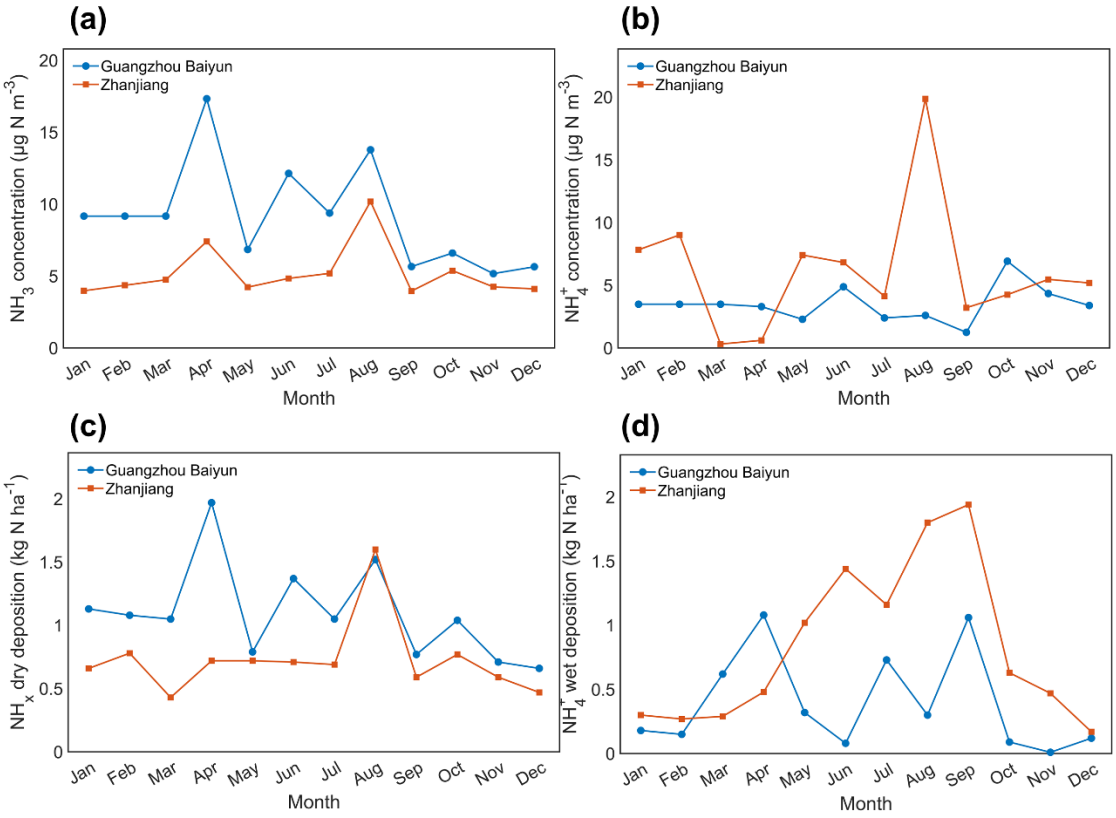

Figure S14. Monthly variation of NH_3 concentration (a), NH_4^+ concentration (b), NHx (NH_3 + NH_4^+) dry deposition fluxes (c), and NH_4^+ wet deposition fluxes (d) in each NNDMN site in

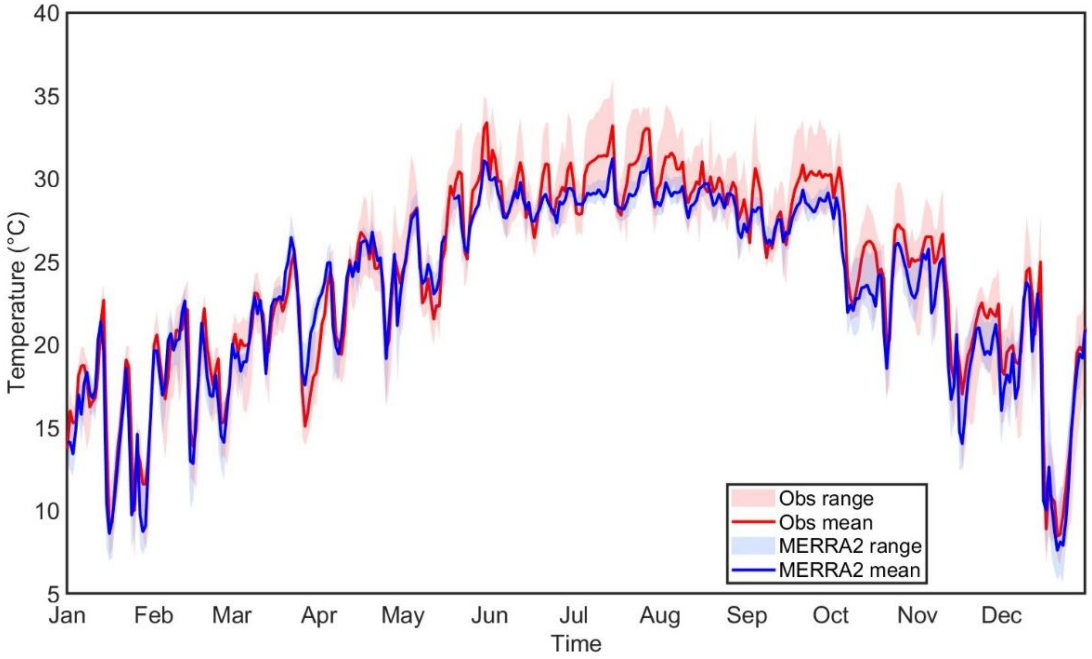

Figure S15. Comparison of daily surface temperature (℃) between the Modern-Era Retrospective analysis for Research and Applications, Version 2 (MERRA-2) reanalysis datasets and surface observations in the Pearl River Delta (PRD) observation network.

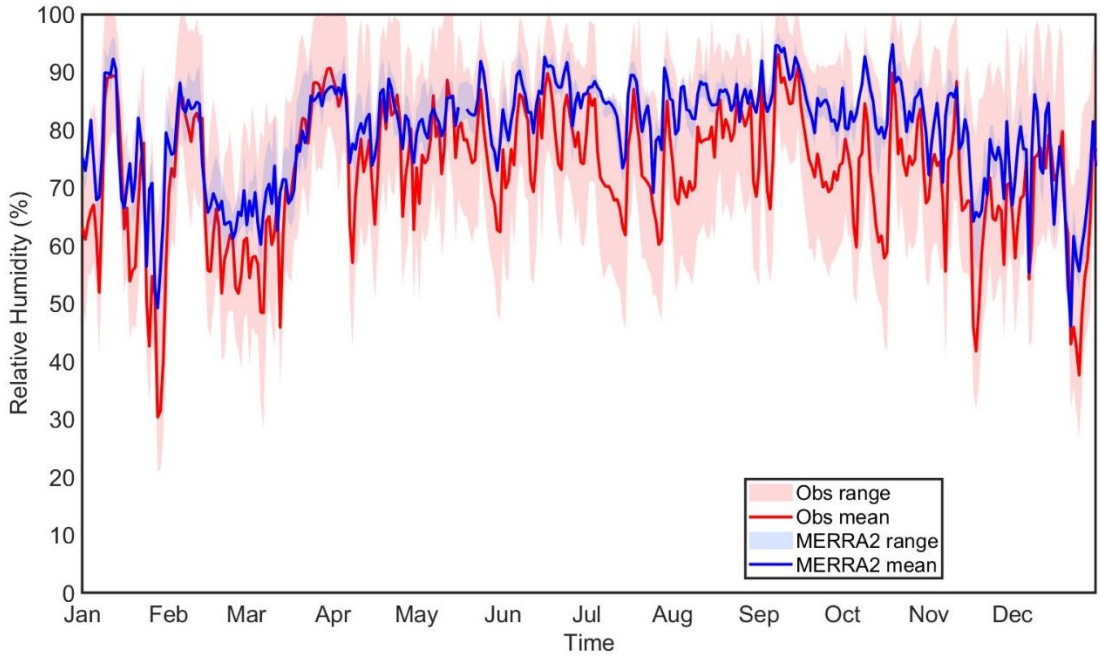

Figure S16. Comparison of daily relative humidity (%) between the Modern-Era Retrospective

analysis for Research and Applications, Version 2 (MERRA-2) reanalysis datasets and surface observations in the Pearl River Delta (PRD) observation network.

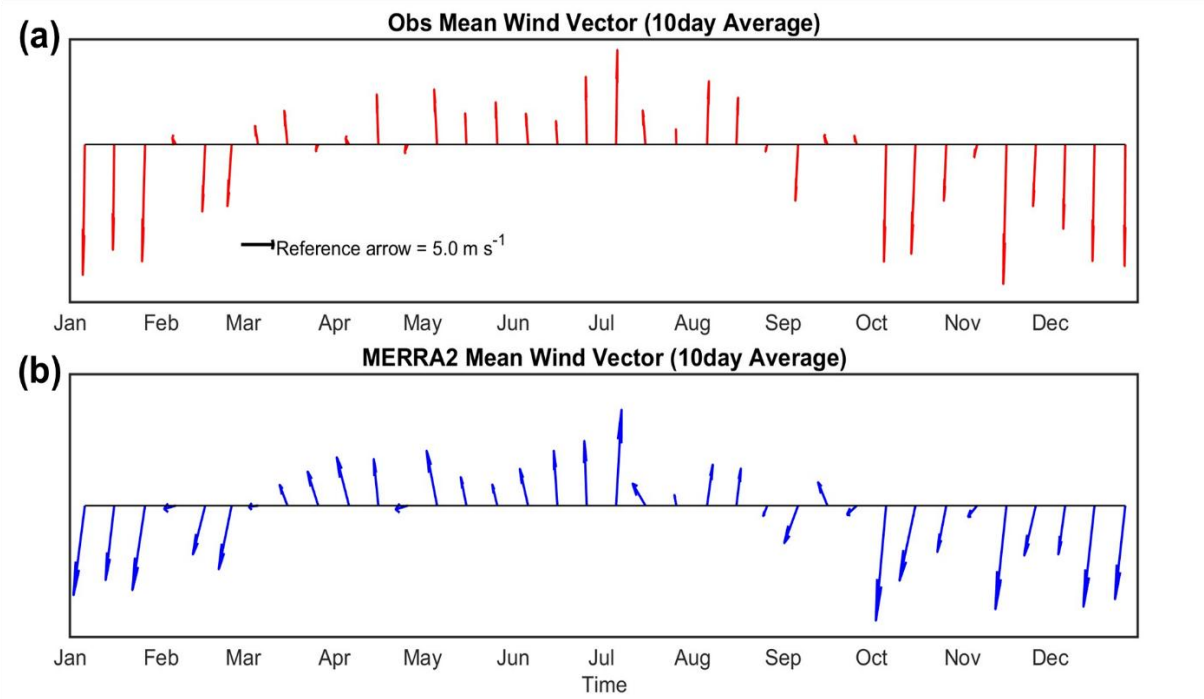

Figure S17. Comparison of 10-day averaged wind speed and direction between the Modern-Era Retrospective analysis for Research and Applications, Version 2 (MERRA-2) reanalysis datasets and surface observations in the Pearl River Delta (PRD) observation network.

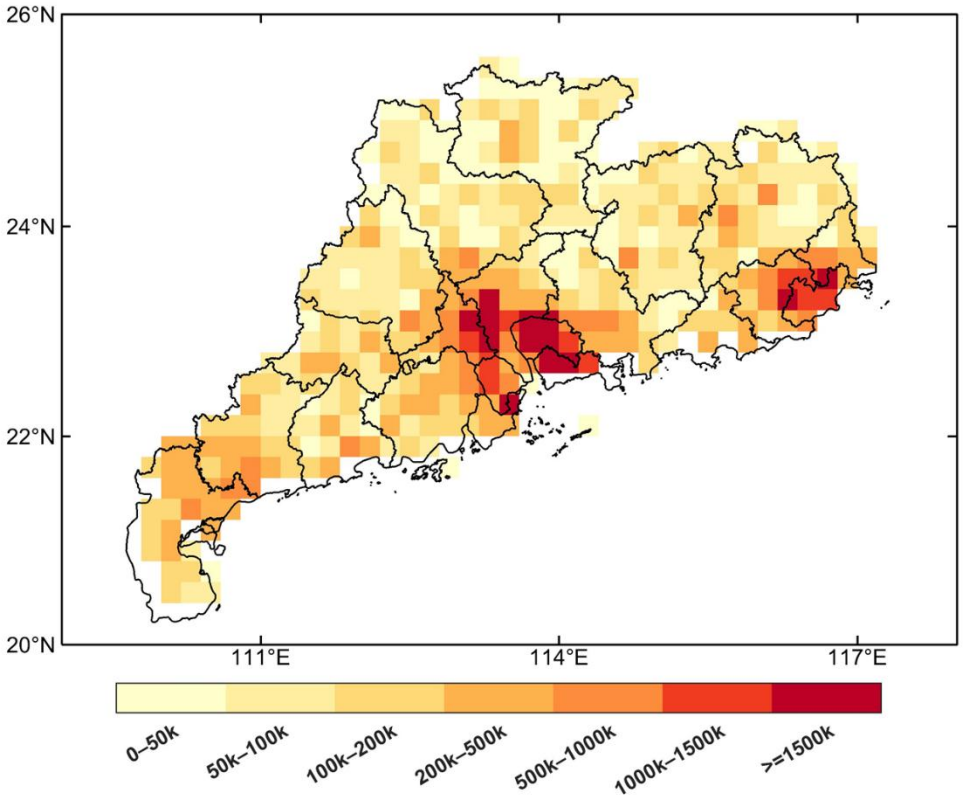

Figure S18. Population distribution in Guangdong in 2023 (population data were obtained from LandScan global high-resolution population dataset, https://landscan.ornl.gov/).

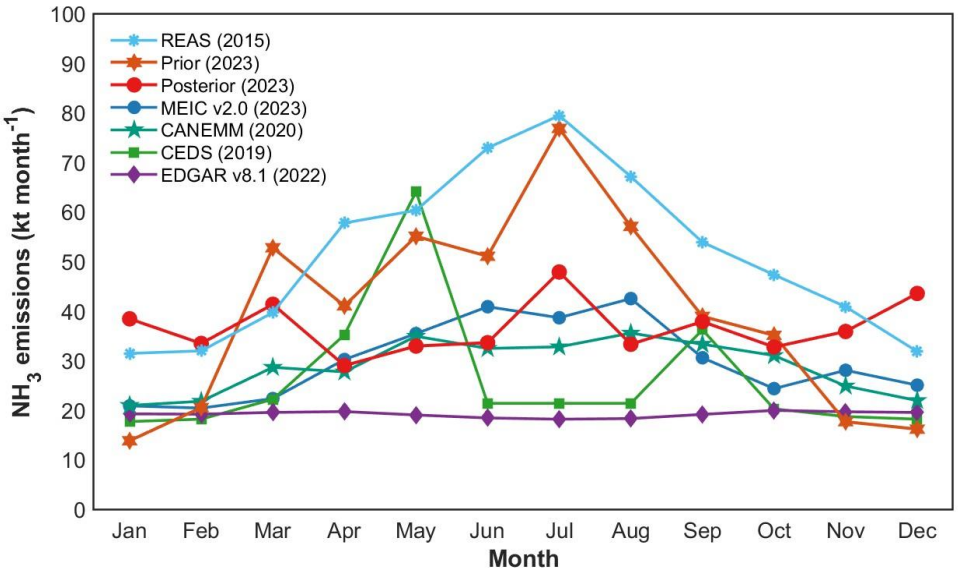

Figure S19. Monthly NH_3 emission variations in Guangdong from prior and posterior estimates in this study and from other published emission inventories (Crippa et al., 2024; Geng et al., 2024; Hoesly et al., 2018; Huang et al., 2012; Kurokawa and Ohara, 2020; Zhang et al., 2018).

Table S1. Full name, locations, and measurement types of the observation sites in the Pearl River Delta (PRD) observation network used in this study.

Code	Full site name	City	Lat	Lon	NH_3	SIA
DXC	Daxuecheng	Guangzhou	23.05	113.39	Y	N
GYQ	Gongyuanqian	Guangzhou	23.13	113.26	Y	Y
LHS	Lianhuashan	Shenzhen	22.56	114.06	Y	N
DC	Dongcheng	Dongguan	23.02	113.79	Y	Y
FSXC	Foshan Xincheng	Foshan	22.97	113.12	Y	N
ZML	Zimaling	Zhongshan	22.51	113.41	Y	N
MH	Meihua	Zhuhai	22.27	113.53	Y	Y
BLSX	Boluo Shixia	Huizhou	23.21	114.03	N	Y
HS	Heshan	Jiangmen	22.71	112.92	N	Y
XQ	Xiqu	Jiangmen	22.59	113.08	Y	N
DZ	Zonghe Guancedian	Zhaoqing	23.07	112.49	Y	Y

Table S2. Detail information of bottom-up inventories that provide NH_3 emissions in Guangdong

Inventory	Cover area	Research period	Spatial resolution	Emission sector
REAS v3.2.1	Asia	1950-2015	0.25° × 0.25°	Power, industry, road transport, off-road transport, residential, fertilizer, livestock and human
MEIC v2.0	China	1990-2023	0.25° × 0.25°	Agriculture, industry, power, residential and transportation
CANEMM	China	2019-2020	0.1° × 0.1°	Fertilizer and livestock
CEDS v2021	Global	1980-2019	0.1° × 0.1°	Agriculture, energy, industry, transportation, residential, solvents, waste and shipping
EDGAR v8.1	Global	1970-2022	0.1° × 0.1°	Agriculture, buildings, industrial combustion, industrial processes, power, transportation, waste and fuel exploitation

References

Bey, I., Jacob, D. J., Yantosca, R. M., Logan, J. A., Field, B. D., Fiore, A. M., Li, Q., Liu, H. Y., Mickley, L. J., and Schultz, M. G.: Global modeling of tropospheric chemistry with assimilated meteorology: Model description and evaluation, Journal of Geophysical Research: Atmospheres, 106, 23073-23095, https://doi.org/10.1029/2001JD000807, 2001.

Burnett, R., Chen, H., Szyszkowicz, M., Fann, N., Hubbell, B., Pope, C. A., Apte, J. S., Brauer, M., Cohen, A., Weichenthal, S., Coggins, J., Di, Q., Brunekreef, B., Frostad, J., Lim, S. S., Kan, H., Walker, K. D., Thurston, G. D., Hayes, R. B., Lim, C. C., Turner, M. C., Jerrett, M., Krewski, D., Gapstur, S. M., Diver, W. R., Ostro, B., Goldberg, D., Crouse, D. L., Martin, R. V., Peters, P., Pinault, L., Tjepkema, M., van Donkelaar, A., Villeneuve, P. J., Miller, A. B., Yin, P., Zhou, M., Wang, L., Janssen, N. A. H., Marra, M., Atkinson, R. W., Tsang, H., Quoc Thach, T., Cannon, J. B., Allen, R. T., Hart, J. E., Laden, F., Cesaroni, G., Forastiere, F., Weinmayr, G., Jaensch, A., Nagel, G., Concin, H., and Spadaro, J. V.: Global estimates of mortality associated with long-term exposure to outdoor fine particulate matter, Proceedings of the National Academy of Sciences, 115, 9592-9597, https://doi.org/10.1073/pnas.1803222115, 2018.

Crippa, M., Guizzardi, D., Pagani, F., Schiavina, M., Melchiorri, M., Pisoni, E., Graziosi, F., Muntean, M., Maes, J., Dijkstra, L., Van Damme, M., Clarisse, L., and Coheur, P.: Insights into the spatial distribution of global, national, and subnational greenhouse gas emissions in the Emissions Database for Global Atmospheric Research (EDGAR v8.0), Earth Syst. Sci. Data, 16, 2811-2830, https://doi.org/10.5194/essd-16-2811-2024, 2024.

Fairlie, T. D., Jacob, D. J., and Park, R. J.: The impact of transpacific transport of mineral dust in the United States, Atmos. Environ., 41, 1251-1266, https://doi.org/10.1016/j.atmosenv.2006.09.048, 2007.

Gelaro, R., McCarty, W., Suárez, M. J., Todling, R., Molod, A., Takacs, L., Randles, C. A., Darmenov, A., Bosilovich, M. G., Reichle, R., Wargan, K., Coy, L., Cullather, R., Draper, C., Akella, S., Buchard, V., Conaty, A., Da Silva, A. M., Gu, W., Kim, G., Koster, R., Lucchesi, R., Merkova, D., Nielsen, J. E., Partyka, G., Pawson, S., Putman, W., Rienecker, M., Schubert, S. D., Sienkiewicz, M., and Zhao, B.: The Modern-Era Retrospective Analysis for Research and Applications, Version 2 (MERRA-2), J. Clim., 30, 5419-5454, https://doi.org/10.1175/JCLI-D-16-0758.1, 2017.

Geng, G., Liu, Y., Liu, Y., Liu, S., Cheng, J., Yan, L., Wu, N., Hu, H., Tong, D., Zheng, B., Yin, Z., He, K., and Zhang, Q.: Efficacy of China's clean air actions to tackle PM2.5 pollution between 2013 and 2020, Nat. Geosci., 17, 987-994, https://doi.org/10.1038/s41561-024-01540-z, 2024.

Hoesly, R. M., Smith, S. J., Feng, L., Klimont, Z., Janssens-Maenhout, G., Pitkanen, T., Seibert, J. J., Vu, L., Andres, R. J., Bolt, R. M., Bond, T. C., Dawidowski, L., Kholod, N., Kurokawa, J., Li, M., Liu, L., Lu, Z., Moura, M. C. P., O'Rourke, P. R., and Zhang, Q.: Historical (1750–2014) anthropogenic emissions of reactive gases and aerosols from the Community Emissions Data System (CEDS), Geosci. Model Dev., 11, 369-408, https://doi.org/10.5194/gmd-11-369-2018, 2018.

Huang, X., Song, Y., Li, M., Li, J., Huo, Q., Cai, X., Zhu, T., Hu, M., and Zhang, H.: A high-resolution ammonia emission inventory in China, Glob. Biogeochem. Cycle, 26,

2011GB004161, https://doi.org/10.1029/2011GB004161, 2012.

Jaeglé, L., Quinn, P. K., Bates, T. S., Alexander, B., and Lin, J. T.: Global distribution of sea salt aerosols: new constraints from in situ and remote sensing observations, Atmos. Chem. Phys., 11, 3137-3157, https://doi.org/10.5194/acp-11-3137-2011, 2011.

Kurokawa, J., and Ohara, T.: Long-term historical trends in air pollutant emissions in Asia: Regional Emission inventory in ASia (REAS) version 3, Atmos. Chem. Phys., 20, 12761-12793, https://doi.org/10.5194/acp-20-12761-2020, 2020.

Liu, H., Jacob, D. J., Bey, I., and Yantosca, R. M.: Constraints from 210Pb and 7Be on wet deposition and transport in a global three-dimensional chemical tracer model driven by assimilated meteorological fields, Journal of Geophysical Research: Atmospheres, 106, 12109-12128, https://doi.org/10.1029/2000JD900839, 2001.

Miller, S. J., Makar, P. A., and Lee, C. J.: HETerogeneous vectorized or Parallel (HETPv1.0): an updated inorganic heterogeneous chemistry solver for the metastable-state NH_4^+–Na^+–Ca^{2+}–K^+–Mg^{2+}–SO_4^{2-}–NO_3^-–Cl^-–H_2O system based on ISORROPIA II, Geosci. Model Dev., 17, 2197-2219, https://doi.org/10.5194/gmd-17-2197-2024, 2024.

Pai, S. J., Heald, C. L., Pierce, J. R., Farina, S. C., Marais, E. A., Jimenez, J. L., Campuzano-Jost, P., Nault, B. A., Middlebrook, A. M., Coe, H., Shilling, J. E., Bahreini, R., Dingle, J. H., and Vu, K.: An evaluation of global organic aerosol schemes using airborne observations, Atmos. Chem. Phys., 20, 2637-2665, https://doi.org/10.5194/acp-20-2637-2020, 2020.

Park, R. J., Jacob, D. J., Field, B. D., Yantosca, R. M., and Chin, M.: Natural and transboundary pollution influences on sulfate-nitrate-ammonium aerosols in the United States: Implications for policy, Journal of Geophysical Research: Atmospheres, 109, https://doi.org/10.1029/2003JD004473, 2004.

Wang, Q., Jacob, D. J., Spackman, J. R., Perring, A. E., Schwarz, J. P., Moteki, N., Marais, E. A., Ge, C., Wang, J., and Barrett, S. R. H.: Global budget and radiative forcing of black carbon aerosol: Constraints from pole-to-pole (HIPPO) observations across the Pacific, J. Geophys. Res.-Atmos., 119, 195-206, https://doi.org/10.1002/2013JD020824, 2014.

Wang, X., Jacob, D. J., Downs, W., Zhai, S., Zhu, L., Shah, V., Holmes, C. D., Sherwen, T., Alexander, B., Evans, M. J., Eastham, S. D., Neuman, J. A., Veres, P. R., Koenig, T. K., Volkamer, R., Huey, L. G., Bannan, T. J., Percival, C. J., Lee, B. H., and Thornton, J. A.: Global tropospheric halogen (Cl, Br, I) chemistry and its impact on oxidants, Atmos. Chem. Phys., 21, 13973-13996, https://doi.org/10.5194/acp-21-13973-2021, 2021.

Wang, Y., Jacob, D. J., and Logan, J. A.: Global simulation of tropospheric O3-NO x - hydrocarbon chemistry: 1. Model formulation, Journal of Geophysical Research: Atmospheres, 103, 10713-10725, https://doi.org/10.1029/98JD00158, 1998.

Zhang, L., Chen, Y., Zhao, Y., Henze, D. K., Zhu, L., Song, Y., Paulot, F., Liu, X., Pan, Y., Lin, Y., and Huang, B.: Agricultural ammonia emissions in China: reconciling bottom-up and top-down estimates, Atmos. Chem. Phys., 18, 339-355, https://doi.org/10.5194/acp-18-339-2018, 2018.